SCIENCE CHINA
Chemistry

•COMMUNICATIONS•

September 2022 Vol.65 No.9: 1715–1719
https://doi.org/10.1007/s11426-022-1318-9

Simple sulfone-bridged heterohelicene structure realizes ultraviolet narrowband thermally activated delayed fluorescence, circularly polarized luminescence, and room temperature phosphorescence

Weimin Ning[1], Han Wang[1], Shaolong Gong[1*], Cheng Zhong[1] & Chuluo Yang[1,2*]

[1]*Department of Chemistry, Hubei Key Lab on Organic and Polymeric Optoelectronic Materials, Wuhan University, Wuhan 430072, China;*
[2]*Shenzhen Key Laboratory of New Information Display and Storage Materials, College of Materials Science and Engineering, Shenzhen University, Shenzhen 518060, China*

Received April 14, 2022; accepted June 24, 2022; published online August 12, 2022

Due to narrowband emission and high quantum efficiencies, polycyclic aromatic heterocycles with multi-resonance thermally activated delayed fluorescence (MR-TADF) properties have recently gained considerable attention in the organic optoelectronic field. Albeit their great promise in the full visible region covering from blue to red, MR-TADF emitters with ultraviolet emission have been rarely reported. Through locking the two *ortho*-positions of a triphenylamine core by sulfone groups, a simple polycyclic aromatic heterocycle, **BTPT**, was facilely constructed, exhibiting 368 nm ultraviolet emission with a narrow full width at half maximum (FWHM) of 33 nm. Its neat film exhibited distinct TADF property with a main emission peak at 388 nm. Noteworthily, the enantiomeric crystals of **BTPT** not only demonstrated significant circularly polarized luminescence (CPL) with large luminescence dissymmetry factor in the 10^{-3} order but also displayed obvious room temperature phosphorescence (RTP). The relationship between this innovative helical unit and unique photophysical properties, including ultraviolet MR-TADF, CPL, and RTP, was reasonably revealed.

polycyclic aromatic heterocycles, thermally activated delayed fluorescence, multi-resonance effect, ultraviolet emission, circularly polarized luminescence, room temperature phosphorescence

Citation: Ning W, Wang H, Gong S, Zhong C, Yang C. Simple sulfone-bridged heterohelicene structure realizes ultraviolet narrowband thermally activated delayed fluorescence, circularly polarized luminescence, and room temperature phosphorescence. *Sci China Chem*, 2022, 65: 1715–1719, https://doi.org/10.1007/s11426-022-1318-9

Polycyclic aromatic hydrocarbons (PAHs) and their heterocyclic analogues have been widely used to construct organic functional materials [1,2], biologically active natural products and pharmaceuticals [3,4] because of their large structure diversity and various functions. Among them, polycyclic aromatic heterocycles containing boron (B) and nitrogen (N) atoms have been an attractive area due to the special position of them in the periodic table. In comparison with the carbon atom, boron has a significantly lower electronegativity and one less electron, while nitrogen has a higher electronegativity and one more electron. Thus, replacement of two carbon atoms by one boron and one nitrogen atom produces polycyclic aromatic heterocycles that are isoelectronic with their all-carbon analogues. Differently, both electronic and optical properties of the B/N doped systems can be selectively tuned by modifying the character of the frontier molecular orbitals and the inter- and/or intramolecular interactions [5–8].

By integrating multiple opposite resonance of B/N atoms through *ortho*-position connection in a rigid polycyclic aromatic heterocycle, Hatakeyama and co-workers [9] demonstrated two emitters with both thermally activated de-

*Corresponding authors (email: slgong@whu.edu.cn; clyang@szu.edu.cn)

layed fluorescence (TADF) property and narrow full width at half maximum (FWHM) in 2016 (Figure 1a, left). Compared with the conventional TADF emitters (Figure 1a, right), the rigid polycyclic aromatic heterocycle can avoid the remarkable structure relaxations in the excited states and thus result in small Stokes shifts and narrow FWHMs in nature. Since then, considerable studies have been made on multi-resonance TADF (MR-TADF) emitters based on specific B/N-based frameworks, especially on the well-known DABNA skeleton [10–16]. However, their complex synthesis and relatively low yields are detrimental to the practical applications of the B/N-based MR-TADF emitters. Several attempts have been proposed to explore the atoms and groups available in MR-TADF emitters. Jiang and co-workers [17] constructed a series of MR-TADF emitters (QAO series) with narrow band emissions by replacing boron atoms with carbonyl groups. Albeit this promising progress, their quantum efficiencies are still far less than B/N-based MR-TADF emitters. In consequence, exploiting novel MR-TADF skeletons with more characteristics and functions is highly desirable.

Nowadays, MR-TADF emitters have validated their potential in the visible region, while MR-TADF emitters with ultraviolet (UV) emission, which have promising potentials in sensor analysis [18], high-density information storage [19], biomedical and forensic applications [20], have been rarely reported [15]. To realize UV emissions, both high S_1 and T_1 energy levels should be guaranteed in TADF molecules, which is extremely difficult for typical D-A structure based TADF emitters that normally have relatively large π-conjugation. By contrast, distorted polycyclic aromatic heterocycles have great promise to realize UV emissions, mainly due to their flexibility in limiting π-conjugation. In addition, helicene derivatives based on distorted polycyclic aromatic heterocycle skeleton have been used as circularly polarized luminescence (CPL) materials that exhibited extensive potential applications in optical quantum information, data storage, chirality sensing, and 3D displays [21–25], whereas no UV-emitting helicene derivative has been reported so far. In addition, multifunctional organic materials with TADF, room temperature phosphorescence (RTP), and CPL simultaneously were rarely reported [26,27]. Therefore, adopting large atoms or groups to produce multiple resonance effect and distorted molecular skeleton in polycyclic aromatic heterocycles could be an alternative to construct UV-emitting multifunctional MR-TADF helicene derivatives.

Herein, we designed and synthesized a pair of chiral MR-TADF enantiomers, (+)-(*P*)-**BTPT** and (−)-(*M*)-**BTPT** (Figure 1c), by using two sulfone groups as the linkage to lock the *ortho*-position of a triphenylamine core to produce the opposite resonance effect in the distorted molecular skeleton (Figure S1, Supporting Information online). Due to the distorted framework, the **BTPT** enantiomers had limited conjugation and helical chirality. Accordingly, the enantiomers exhibited narrowband ultraviolet emission both in solution and film, together with a distinct TADF property in film state. Inspiringly, the enantiomers (+)-(*P*)-**BTPT** and (−)-(*M*)-**BTPT** displayed mirror-image circular dichroism (CD) spectra in solution and their enantiomeric crystals exhibited obvious mirror-image CPL with large luminescence dissymmetry factor (g_{lum}) of 10^{-3} order. Besides, the **BTPT** crystals displayed strong RTP emission in the blue region.

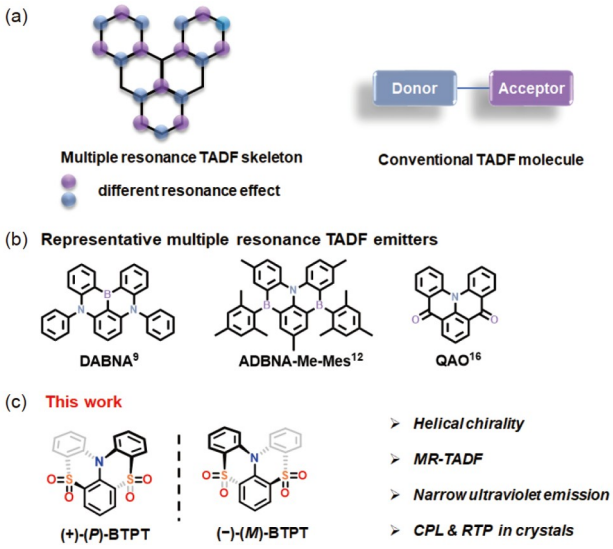

Figure 1 (a) Design strategies for TADF molecules; (b) representative multiple resonance TADF emitters; (c) chemical structures and main characters of **BTPT** (color online).

The synthetic route of **BTPT** was shown in Scheme S1 (Supporting Information online). Intermediate compound **1** (benzo[5,6][1,4]thiazino[2,3,4-kl]phenothiazine) was oxidized without a metal catalyst to afford **BTPT** with an extremely high yield of 92%. This simple and effective synthetic route significantly outperformed the reported synthesis of classic B/N-based MR-TADF systems. The target compound **BTPT** was purified by column chromatography and temperature-gradient vacuum sublimation and its chemical structure was fully characterized by nuclear magnetic resonance, mass spectrometry and single-crystal diffraction. **BTPT** exhibited high thermal stability with a high decomposition temperature (T_d, corresponding to 5% weight loss) of 330 °C and a glass transition temperature (T_g) of 75 °C (Figure S5). **BTPT** experienced irreversible oxidation and reduction processes, together with the highest occupied molecular orbital (HOMO) and lowest unoccupied molecular orbital (LUMO) levels of −6.7 and −2.7 eV, respectively (Figure S6).

The enantiomers, (+)-(*P*)-**BTPT** and (−)-(*M*)-**BTPT**, were obtained *via* the optical resolution of racemates by chiral high-performance liquid chromatography (HPLC). The ab-

solute configurations of the enantiomers were confirmed by the single-crystal diffraction (Figure 2). Furthermore, their specific rotation ($[\alpha_D^{25}]$) were measured to be +159° and –254° for (+)-(*P*)-**BTPT** and (−)-(*M*)-**BTPT**, respectively. To evaluate the stability of the chiral configuration, the racemization energy barrier and conversion temperature were calculated to be 32 kcal/mol and 434 K (Figure S9B), respectively, indicating the stability of chiral configuration at room temperature. In the enantiomer crystals, longer C–S bonds (1.74–1.75 Å) compared with C–N bonds (1.40–1.44 Å) and tetrahedral configuration of sulfonyl linkage gave rise to the large distortion and stable chiral configuration. In addition, the steric hindrance between adjacent hydrogen atoms in two different peripheral benzene rings, such as **H5** and **H8** in (+)-(*P*)-**BTPT**, played an important role in stabilizing chiral configuration. All these factors resulted in a large dihedral angle of ~61° between the peripheral benzene rings, which was larger than those of [5]helicene (46°) and [6]helicene (58°) molecules [28,29].

Subsequently, photophysical properties of the enantiomers in the monomolecular state were characterized. The characterization of (+)-(*P*)-**BTPT** was taken as an example. As shown in Figure 3a, the UV-visible absorption spectra of (+)-(*P*)-**BTPT** in diluted toluene (1×10^{-5} M) exhibited a sharp absorption band with a maxima at 346 nm, which should be ascribed to the short-range charge transfer of the **BTPT** framework. In diluted toluene at room temperature, (+)-(*P*)-**BTPT** exhibited intensely ultraviolet emission at 368 nm with a small FWHM of 33 nm. To further explore the emission transition characteristics, we measured the emission spectra of (+)-(*P*)-**BTPT** in different solvents at room temperature. Typical solvatochromic effect was observed with the increasing solvent polarity from hexane to dimethylformamide, indicating the charge transfer characteristic of S_1 for (+)-(*P*)-**BTPT** (Figure S8a). Hereafter, CD spectra of the enantiomers in dilute solution were investigated to further characterize the chiroptical properties. Obvious mirror-image CD spectra of the enantiomers were observed (Figure 3b), and their mirror-image CD spectra remained the same after heating at 65 °C for 20 min, testifying the stable chiral configuration of (+)-(*P*)-**BTPT** (Figure S9b). In 1 wt% doped polymethyl methacrylate (PMMA) film, (+)-(*P*)-**BTPT** exhibited almost identical fluorescence (300 K) and phosphorescence spectra (77 K) with the main emission peaks at around 401 nm and thus the energy levels of S_1 and T_1 states were estimated to be 3.46 and 3.32 eV, according to the onset of emission spectra (Figure 3c). The small ΔE_{ST} (0.14 eV) was conducive to access TADF property. As expected, (+)-(*P*)-**BTPT** in the PMMA film at room temperature displayed distinct delayed fluorescence component together with the fitting lifetime of 109 μs (Figure 3d). Moreover, the delayed fluorescence component of the transient PL gradually increased with the increasing temperature from 100 to 300 K (Figure S8b), confirming the thermal activation mechanism of the delayed fluorescence.

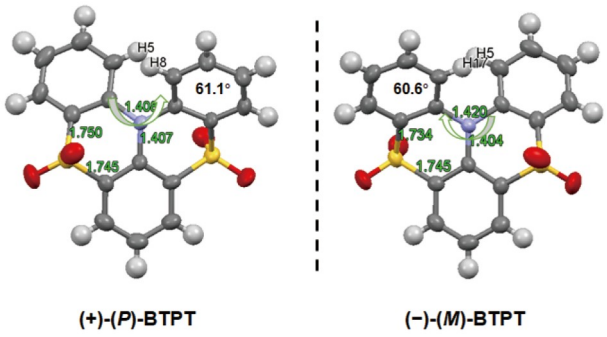

Figure 2 Single-crystal structures of (+)-(*P*)-**BTPT** and (−)-(*M*)-**BTPT** (color online).

Interestingly, the spin-coated neat film of (+)-(*P*)-**BTPT** exhibited a narrow ultraviolet emission peaking at 388 nm, coupled with a relatively small FWHM of 50 nm (Figure 3e). Compared with the PMMA doped film, the neat film displayed a redshifted phosphorescence spectrum, which may come from the greater environmental polarity and lower T_1 state of dimer aggregation in neat film [30]. The spin-coated neat film of (+)-(*P*)-**BTPT** also experienced obvious delayed fluorescence with the fitting of 112 μs at room temperature, accompanied by the positive temperature-dependent delayed fluorescence component up on the increasing temperature from 100 to 300 K (Figure 3f). These results clearly certified the TADF property of (+)-(*P*)-**BTPT** in the film state. In addition, (−)-(*M*)-**BTPT** displayed almost identical optical properties as (+)-(*P*)-**BTPT** in the monomolecular and film states.

Surprisingly, the enantiomeric crystals displayed significant CPL signal with remarkable g_{lum} values of -2.8×10^{-3} and $+7.8\times10^{-3}$, respectively (Figure 4a, b). The CPL spectral profiles were consistent with the fluorescence spectra of the enantiomeric crystals, indicating the CPL signal came from the enantiomeric crystals. To figure out the origin of the distinct CPL, CD spectrum of the enantiomer crystal was measured. As shown in Figure S10a, a new peak at around 370 nm with the negative Cotton effect was observed for the (+)-(*P*)-**BTPT** crystals, with respect to its CD spectrum in solution. This is consistent with the negative signal in CPL spectrum of the (+)-(*P*)-**BTPT** crystals, although no CPL signal was detected for (+)-(*P*)-**BTPT** in solution. The above results indicated the emerging negative CD peak could account for the CPL spectra of crystals [31–33]. Moreover, the simulated ECD spectrum that testified the emerging negative CD peak may originate from the dimer structure in the crystals (Figure S10b), which further assemble to form 3D helical structure and thus amplify the g_{lum} value (Figure 4d). Right-handed (+)-(*P*)-**BTPT** crystal was taken as an example (Figure 4d). Firstly, two adjacent homochiral molecules

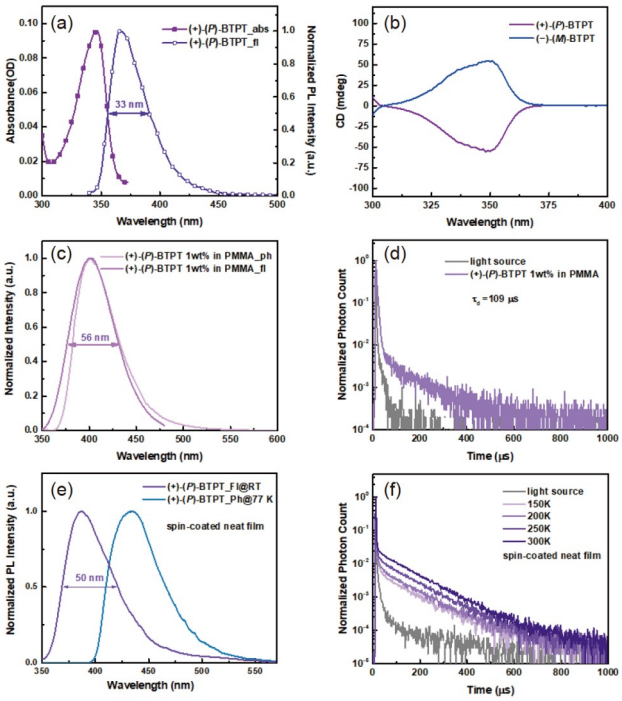

Figure 3 (a) Absorption and normalized fluorescence spectra of (+)-(*P*)-**BTPT** in dilute toluene (1×10^{-5} M); (b) CD spectra of enantiomers in dilute dichloromethane (1×10^{-3} M); (c) normalized fluorescence (300 K) and phosphorescence spectra (77 K) of (+)-(*P*)-**BTPT** in 1 wt% doped PMMA film; (d) transient photoluminescence spectra of (+)-(*P*)-**BTPT** in 1 wt% doped PMMA film; (e) normalized fluorescence (300 K) and phosphorescence spectra (77 K) of (+)-(*P*)-**BTPT** spin-coated neat film; (f) temperature-dependent transient photoluminescence spectra of (+)-(*P*)-**BTPT** spin-coated neat film (color online).

along *b*-axis formed a pair of right-handed helical dimer *via* S=O···H interactions (~2.7 and ~2.5 Å). Secondly, those dimers were arranged in a right-handed spiral column along *b*-axis *via* weak S=O···π interactions (~3.1 Å), introducing a larger helical structure compared with the single molecule and helical dimers. Finally, (+)-(*P*)-**BTPT** molecules constructed a regular plane in the *a*-*c* plane through abundant S=O···H interactions (~2.4 and ~2.7 Å) and thus restrained the orientation of the helical axis. On the other hand, the (−)-(*M*)-**BTPT** crystal also had similar features to generate a left-handed helical structure. All these features of the enantiomeric crystals realized the significant CPL spectra with the considerable g_{lum} values.

Unexpectedly, both enantiomeric crystals exhibited obvious RTP emission at the blue region. To illustrate, the (+)-(*P*)-**BTPT** crystal displayed distinct RTP emission with a maxima peak at 458 nm together with a fitting lifetime (τ_{RTP}) of 13.7 ms (Figure 5). To figure out the origin of the RTP emission, we carried out the hole-electron analysis on T_1 of the (+)-(*P*)-**BTPT** molecule. As shown in Figure S13, dimers in the (+)-(*P*)-**BTPT** crystal exhibited a mainly single molecule participated T_1 with large spin-orbital coupling constant (ξ_{st}) between S_0 and T_1 (~0.8 cm^{-1}) which was large enough to satisfy the transition from T_1 to S_0. Like other

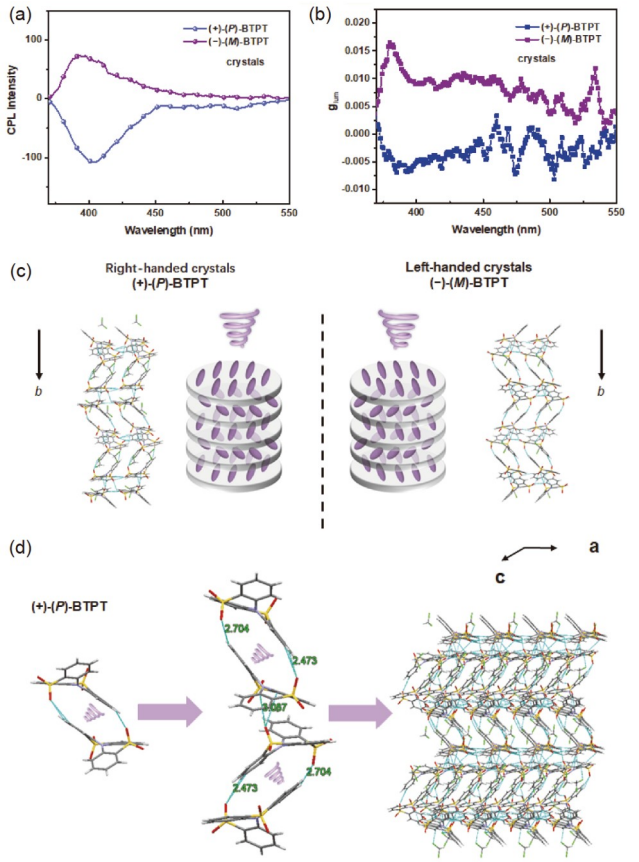

Figure 4 (a) CPL spectra and (b) g_{lum} values of enantiomeric crystals; (c) the schematic of CPL in crystals; (d) helical structures in enantiomeric crystals (color online).

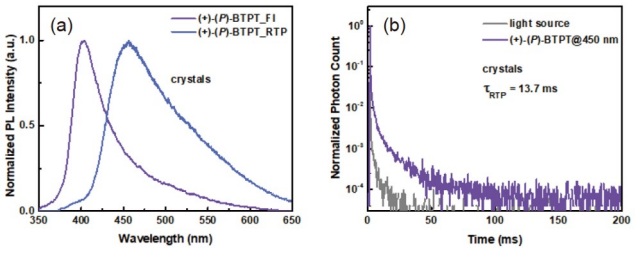

Figure 5 (a) Normalized fluorescence (300 K) and phosphorescence (300 K) spectra of the (+)-(*P*)-**BTPT** crystal; (b) transient photoluminescence spectrum of the (+)-(*P*)-**BTPT** crystal (color online).

phenothiazine oxide derivatives [34–36], the introducing of sulfone groups effectively promoted the intersystem crossing from S_1 to T_1, making it efficient for the accumulation of T_1. Moreover, the hole-electron analysis was conducted to figure out the transition nature of S_1 and T_1. As shown in Figure S11, S_1 was dominated by the charge transfer (CT) feature while T_1 has dominant π-π* character. Such significant difference between S_1 and T_1 states could benefit ISC from S_1 to T_1 according to the El-Sayed rule. On the other hand, the rigid molecular configuration and abundant intermolecular interactions (abundant S=O···H interactions and S=O···π

interactions, Figure 4 and Figure S7) in the crystal could not only effectively isolate water and oxygen in the air, but also restrict the non-radiative decay from T_1 to S_0. These factors induced the RTP emission from T_1 mainly dominated by the single molecule of (+)-(*P*)-BTPT. Similarly, the RTP emission in the (−)-(*M*)-**BTPT** crystal mainly originated from the single molecule of (−)-(*M*)-**BTPT**.

In summary, a multifunctional polycyclic aromatic heterocycle **BTPT** has been developed. It exhibited narrow ultraviolet emission with obvious TADF property in neat film and displayed apparent RTP emission and significant CPL signal with considerable g_{lum} in crystals. The single-crystal analysis revealed that tetrahedral configuration of sulfonyl linkage, longer C–S bonds than C–N bonds, and steric hindrance between adjacent peripheral benzene rings were the key point to stabilize the chiral configurations of the enantiomers. Interestingly, multistage helical structures in enantiomeric crystals of **BTPT** resulted in distinct CPL with the large average g_{lum} values in emission region (-2.8×10^{-3} and $+7.8\times10^{-3}$ for *P*- and *M*-configurations, respectively). Moreover, sulfone groups and abundant intermolecular interactions induced significant RTP emission in crystals. This work not only expands the species of TADF emitters with ultraviolet emission but also widens the scope of available building blocks for multifunctional polycyclic aromatic heterocycles with MR-TADF, CPL, and RTP simultaneously.

Acknowledgements This work was supported by the National Natural Science Foundation of China (52022071, 52130308, 91833304), the Fundamental Research Funds for the Central Universities (2042021kf1060), and Shenzhen Science and Technology Program (ZDSYS20210623091813040, JCYJ20190808151209557). The numerical calculations in this paper have been done on the supercomputing system in the Supercomputing Center of Wuhan University.

Conflict of interest The authors declare no conflict of interest.

Supporting information The supporting information is available online at http://chem.scichina.com and http://link.springer.com/journal/11426. The supporting materials are published as submitted, without typesetting or editing. The responsibility for scientific accuracy and content remains entirely with the authors.

1 Wu B, Jiang L, Luo Y, Wang C. *Angew Chem Int Ed*, 2020, 59: 3942–3947
2 Qu J, Dai XX, Cui JS, Chen RX, Wang X, Lin YH, Verduzco R, Wang HL. *J Mater Chem A*, 2021, 9: 16554–16564
3 Chambers GE, Sayan AE, Brown RCD. *Nat Prod Rep*, 2021, 38: 1794–1820
4 Ren K, Wei Y, Li J, Han C, Deng Y, Su G. *Chemosphere*, 2021, 283: 131190
5 Hirai M, Tanaka N, Sakai M, Yamaguchi S. *Chem Rev*, 2019, 119: 8291–8331
6 Pati PB, Jin E, Kim Y, Kim Y, Mun J, Kim SJ, Kang SJ, Choe W, Lee G, Shin HJ, Park YS. *Angew Chem Int Ed*, 2020, 59: 14891–14895
7 Chen Y, Chen W, Qiao Y, Lu X, Zhou G. *Angew Chem Int Ed*, 2020, 59: 7122–7130
8 Gotoh H, Nakatsuka S, Tanaka H, Yasuda N, Haketa Y, Maeda H, Hatakeyama T. *Angew Chem Int Ed*, 2021, 60: 12835–12840
9 Hatakeyama T, Shiren K, Nakajima K, Nomura S, Nakatsuka S, Kinoshita K, Ni J, Ono Y, Ikuta T. *Adv Mater*, 2016, 28: 2777–2781
10 Kondo Y, Yoshiura K, Kitera S, Nishi H, Oda S, Gotoh H, Sasada Y, Yanai M, Hatakeyama T. *Nat Photonics*, 2019, 13: 678–682
11 Ahn DH, Kim SW, Lee H, Ko IJ, Karthik D, Lee JY, Kwon JH. *Nat Photonics*, 2019, 13: 540–546
12 Oda S, Kawakami B, Kawasumi R, Okita R, Hatakeyama T. *Org Lett*, 2019, 21: 9311–9314
13 Yang M, Park IS, Yasuda T. *J Am Chem Soc*, 2020, 142: 19468–19472
14 Qi Y, Ning W, Zou Y, Cao X, Gong S, Yang C. *Adv Funct Mater*, 2021, 31: 2102017
15 Suresh SM, Duda E, Hall D, Yao Z, Bagnich S, Slawin AMZ, Bässler H, Beljonne D, Buck M, Olivier Y, Köhler A, Zysman-Colman E. *J Am Chem Soc*, 2020, 142: 6588–6599
16 Chen F, Zhao L, Wang X, Yang Q, Li W, Tian H, Shao S, Wang L, Jing X, Wang F. *Sci China Chem*, 2021, 64: 547–551
17 Yuan Y, Tang X, Du X, Hu Y, Yu Y, Jiang Z, Liao L, Lee S. *Adv Opt Mater*, 2019, 7: 1801536
18 Shinar J, Shinar R. *J Phys D-Appl Phys*, 2008, 41: 133001
19 Kishi H, Mizuno Y, Chazono H. *Jpn J Appl Phys*, 2003, 42: 1–15
20 Manna E, Fungura F, Biswas R, Shinar J, Shinar R. *Adv Funct Mater*, 2015, 25: 1226–1232
21 Farshchi R, Ramsteiner M, Herfort J, Tahraoui A, Grahn HT. *Appl Phys Lett*, 2011, 98: 162508
22 Yang Y, da Costa RC, Fuchter MJ, Campbell AJ. *Nat Photon*, 2013, 7: 634–638
23 Warning LA, Miandashti AR, McCarthy LA, Zhang Q, Landes CF, Link S. *ACS Nano*, 2021, 15: 15538–15566
24 Yang Y, da Costa RC, Smilgies DM, Campbell AJ, Fuchter MJ. *Adv Mater*, 2013, 25: 2624–2628
25 Gong ZL, Zhu X, Zhou Z, Zhang SW, Yang D, Zhao B, Zhang YP, Deng J, Cheng Y, Zheng YX, Zang SQ, Kuang H, Duan P, Yuan M, Chen CF, Zhao YS, Zhong YW, Tang BZ, Liu M. *Sci China Chem*, 2021, 64: 2060–2104
26 Data P, Takeda Y. *Chem Asian J*, 2019, 14: 1613–1636
27 Takeda Y, Data P, Minakata S. *Chem Commun*, 2020, 56: 8884–8894
28 Berezhnaia V, Roy M, Vanthuyne N, Villa M, Naubron JV, Rodriguez J, Coquerel Y, Gingras M. *J Am Chem Soc*, 2017, 139: 18508–18511
29 Martin RH. *Angew Chem Int Ed*, 1974, 13: 649–660
30 An Z, Zheng C, Tao Y, Chen R, Shi H, Chen T, Wang Z, Li H, Deng R, Liu X, Huang W. *Nat Mater*, 2015, 14: 685–690
31 Wang Y, Harada T, Phuong LQ, Kanemitsu Y, Nakano T. *Macromolecules*, 2018, 51: 6865–6877
32 Kinuta T, Sato T, Nakano Y, Harada T, Tajima N, Fujiki M, Kuroda R, Matsubara Y, Imai Y. *J Photochem Photobiol A-Chem*, 2011, 220: 134–138
33 Mimura Y, Nishikawa T, Fuchino R, Nakai S, Tajima N, Kitamatsu M, Fujiki M, Imai Y. *Org Biomol Chem*, 2017, 15: 4548–4553
34 Yang J, Gao H, Wang Y, Yu Y, Gong Y, Fang M, Ding D, Hu W, Tang BZ, Li Z. *Mater Chem Front*, 2019, 3: 1391–1397
35 Tian Y, Yang J, Liu Z, Gao M, Li X, Che W, Fang M, Li Z. *Angew Chem Int Ed*, 2021, 60: 20259–20263
36 Yang J, Zhen X, Wang B, Gao X, Ren Z, Wang J, Xie Y, Li J, Peng Q, Pu K, Li Z. *Nat Commun*, 2018, 9: 840